ELSEVIER

Journal of Hazardous Materials 132 (2006) 14–25

Journal of Hazardous Materials

www.elsevier.com/locate/jhazmat

Lidar characterization of crystalline silica generation and transport from a sand and gravel plant

Krystyna Trzepla-Nabaglo [a], Ryoji Shiraki [b], Britt A. Holmén [c,*]

[a] *Crocker Nuclear Laboratory, University of California, Davis, One Shields Ave., Davis, CA 95616, USA*
[b] *University of California, Davis, McClellan Nuclear Radiation Center, 5335 Price Avenue, McClellan, CA 95652, USA*
[c] *Civil & Environmental Engineering, University of Connecticut, 261 Glenbrook Road, Unit 2037, Storrs, CT 06269-2037, USA*

Available online 18 January 2006

Abstract

Light detection and ranging (Lidar) remote sensing two-dimensional vertical and horizontal scans collected downwind of a sand and gravel plant were used to evaluate the generation and transport of geologic fugitive dust emitted by quarry operations. The lidar data give unsurpassed spatial resolution of the emitted dust, but lack quantitative particulate matter (PM) mass concentration data. Estimates of the airborne PM_{10} and crystalline silica concentrations were determined using linear relationships between point monitor PM_{10} and quartz content data with the lidar backscatter signal collected from the point monitor location. Lidar vertical profiles at different distances downwind from the plant were used to quantify the PM_{10} and quartz horizontal fluxes at 2-m vertical resolution as well as off-site emission factors. Emission factors on the order of 65–110 kg of PM_{10} (10–30 kg quartz) per daily truck activity or 2–4 kg/t product shipped (0.5–1 kg quartz/t) were quantified for this facility. The lidar results identify numerous elevated plumes at heights >30 m and maximum plume heights of 100 m that cannot be practically sampled by conventional point sampler arrays. The PM_{10} and quartz mass flux was greatest at 10–25 m height and decreased with distance from the main operation. Measures of facility activity were useful for explaining differences in mass flux and emission rates between days. The study results highlight the capabilities of lidar remote sensing for determining the spatial distribution of fugitive dust emitted by area sources with intermittent and spatially diverse dust generation rates.

Keywords: Fugitive dust; PM_{10}; Quartz; Emission factor; Lidar

1. Introduction

It has been widely accepted that the inhalation of two crystalline silica (CS) polymorphs, quartz, and cristobalite, causes diseases such as lung cancer and silicosis, although the exact mechanisms of these adverse health effects are still controversial [1–3]. In 1997, the International Agency for Research on Cancer (IARC) upgraded these minerals to Group 1 status (carcinogenic to humans) [4]. Quarries, mines, construction/demolition, and industrial manufacturers are major sources for airborne quartz particles, whereas diatomaceous earth production and ceramic and pottery industries are sources of cristobalite. It is essential to quantify the atmospheric load of respirable CS emitted from these stationary sources in order to evaluate the risk of human exposure to these toxic materials.

Despite the importance of airborne CS, only a limited number of studies have measured quartz concentrations in airborne dust [5–7]. Reported values at ambient monitoring stations in urban cities were non-detect to 1.9 $\mu g\,m^{-3}$ for $PM_{2.5}$ and 0.9–8.0 $\mu g\,m^{-3}$ for PM_{15} in 22 US cities [6], 0.6–1.5 $\mu g\,m^{-3}$ for PM_{10} in Rome, Italy [7], and 9.6–16.1 wt% for high-volume filter samples, and 10.4–21.7 wt% for low-volume filter samples in an industrial area of Utah [5]. For different types of California agricultural operations, the average quartz mass concentration in dust was estimated to be 365 $\mu g\,m^{-3}$ for inhalable (7–20 μm diameter) dust and 97 $\mu g\,m^{-3}$ for respirable (0.5–7 μm diameter) dust [8]. We have previously studied dry season quartz concentrations in PM_{10} collected upwind and downwind of a sand and gravel quarry in California and found that the air quality of the most remote sampling site located about 750 m downwind was still impacted by the facility's activity (9.4

* Corresponding author. Tel.: +1 860 486 3941; fax: +1 860 486 2298.
E-mail address: baholmen@engr.uconn.edu (B.A. Holmén).

0304-3894/$ – see front matter © 2005 Elsevier B.V. All rights reserved.
doi:10.1016/j.jhazmat.2005.11.092

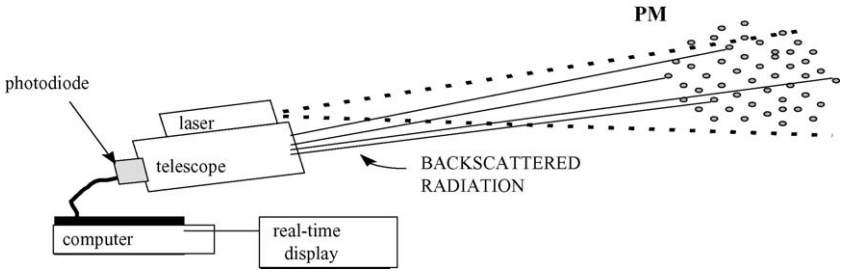

Fig. 1. Schematic of elastic lidar instrument principle.

(± 0.9) $\mu g\,m^{-3}$ compared to 4.6 (± 0.9) $\mu g\,m^{-3}$ at the upwind site) [9]. The present study expands upon our previous work by incorporating lidar remote sensing for detection and better spatial characterization of the fugitive dust emitted by the quarry operations.

Lidar is an acronym for light detection and ranging. Lidar systems use a laser beam transmitter to scan through the atmosphere over a desired range of horizontal azimuth directions and vertical elevations. In elastic lidar, the 180° backscattered light is collected by a telescope receiver and is measured with a photodetector (Fig. 1). The signal is digitized to create a real-time image of the gas and particle relative backscatter within the scanned region.

Because Rayleigh scattering due to atmospheric gas molecules ($\sim 1/\lambda^4$) (where λ is the wavelength of light) is insignificant relative to particle backscatter at the 1 μm wavelength, the lidar signal gives particle attenuation (extinction + backscatter) information directly. By assuming a relationship between particle backscatter and particle mass or number, the lidar signal can be used in a semi-quantitative manner to monitor and track particle concentrations with high temporal (1 s) and spatial (5 m) resolution that cannot be achieved with point PM samplers. In this study, relationships between the 1.064 μm lidar signal and PM_{10} mass concentration measured gravimetrically are used to estimate vertical profiles of the PM_{10} and corresponding quartz mass flux.

The return power received by the lidar from a given range R, $P(R)$:

$$P(R) = P_o \kappa \frac{\beta(R)}{R^2} \exp\left[-2\int_0^R \alpha(r)\,dr\right] \quad (1)$$

is a function of the outgoing laser power [P_o, W], the volume backscatter coefficient [$\beta(R)$, $m^{-1}\,sr^{-1}$], the volume extinction coefficient [$\alpha(r)$, m^{-1}], and κ is the lidar calibration constant. The lidar signal is a function of both the quantity of particles detected as well as the backscattering efficiency of the individual particles. Particle backscatter is a function of particle composition, size, and shape; therefore, variations in any of these parameters will affect the lidar signal. For soil-derived PM, variations in particle size and particle number will be the dominant factors affecting the lidar return signal at a given field site. Because backscattered light intensity is a strong function of particle size relative to the wavelength of the incident light [10], particles with diameters close to the laser's wavelength will scatter more light back to the lidar than larger particles, which tend to forward-scatter the light [10–12]. Based on Mie theory, the 1.064 μm wavelength of the lidar used in this study means particles between 0.5 and 5 μm diameter are responsible for most of the detected signal; these particles are collected in PM_{10} point samplers.

Previous studies have typically provided data on CS concentrations at a single height at each sampling location [5–8]. By combining the spatial resolution capabilities of lidar techniques with our PM_{10} sample quartz concentrations determined by X-ray diffraction of filter samples [9], the present study expands upon previous work in order to characterize the vertical distribution of PM_{10} and CS downwind of a sand and gravel quarry. These techniques provide the first estimates of the quartz flux and emission rate as a function of distance from the operation that are essential for full understanding of downwind receptor exposure.

2. Experimental methods

2.1. Field PM mass sampling

Field PM measurements were made at one location upwind (U1) and four locations downwind (D1, D2, D3, and D4) of sand and gravel processing operations in Northern California (Fig. 2). PM_{10} and $PM_{2.5}$ were collected on 25 mm stretched Teflon filters (3 μm Teflo®, Gelman R2P1025) using Interagency Monitoring of Protected Visual Environments (IMPROVE) aerosol samplers [13,14]. The PM samplers at the five locations were sampled in eight separate test periods between June 13 and June 21, 2000; only the data for June 13–16 are included here because these days had corresponding lidar data. The sampling height was 3 m from the ground at all PM sampler locations.

2.1.1. Meteorological measurements

A 10-m tower was erected upwind of most of the plant activity in order to collect meteorological data. The tower was equipped with Met One 014A anemometers to measure wind speed and Campbell Scientific 107 Air Temperature probes at heights of 1, 2, 4, and 7.5 m and a Vaisala HMP35C temperature and relative humidity probe at 2 m. Wind direction and solar radiation were measured at 4 m using a Met One 024A Wind Vane and a Campbell Scientific LI200X Pyranometer, respectively. The instruments were polled every second by a Campbell Scientific CR-10 data logger, and 1 min averages were stored for later analysis.

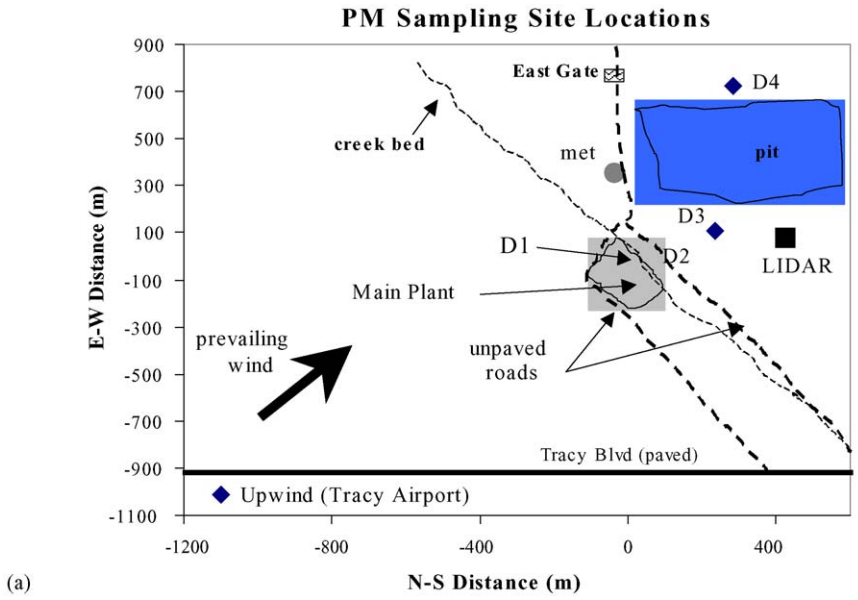

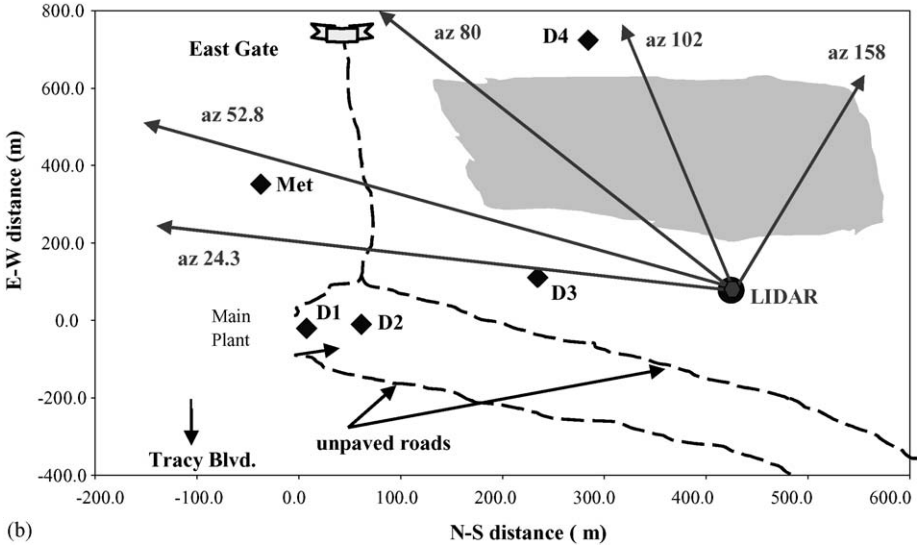

Fig. 2. (a) Relative locations of the PM sampling locations at the sand and gravel facility. The origin of the coordinate system (0, 0) was the pile of road base product material that was sampled for soils analysis and PM_{10} resuspension. E/W–N/S coordinates of each PM sampler, the lidar and the meteorological tower were: U1 (−1013.4, 1099.2), D1 (−20.7, −7.5), D2 (−10.2, −61.5), D3 (110.5, −234.5), D4 (604.7, −436), meteorological tower "Met" (351.8, 37.4) and lidar (424.5, 77.5). The shaded area around site D1 encompasses the Main Plant where conveyor/separating/crushing equipment and product piles were located. (b) Arrows indicate lidar azimuths relative to the PM sampling site locations in (a).

2.1.2. Site activity during field sampling

The plant operators provided the facility activity data in Table 1 for the days field sampling occurred. Daily truck and product shipped values were subdivided into activity at the aggregate plant and the asphalt plant. The aggregate plant (Main Plant) was the focus of the crystalline silica study, but trucks traveling to/from the asphalt plant on the site's unpaved roads may have generated road dust containing CS.

2.2. X-ray diffraction (XRD) for quartz determination in PM_{10} samples

Data on the quartz mass fraction of PM_{10} were taken from Shiraki and Holmén [9]. Briefly, PM samples were removed from the stretched Teflon filters via sonication in propanol and were redeposited within an area of 10 mm × 10 mm on silver membrane filters. This area corresponds to the size of the X-ray beam at $2\theta = 26.6°$, the 2θ position for the quartz primary peak, on the Rigaku Miniflex diffractometer used for quantitative analysis. Sample mass was determined by difference in weight of the filter before and after deposition. In similar way, calibration standards were prepared using NIOSH standard Q-1 (alpha quartz). The quartz primary peak was measured using a 0.01° step scan (30 s/step) from $2\theta = 26.0°$ to 27.5° using Cu Kα radiation generated at 30 kV and 10 mA. The peak intensity was determined as the peak area above the baseline and the mean peak area for four sample orientations was used for all calculations. The mass fraction of quartz in field samples was

Table 1
Sand and gravel facility activity data

Date	Trucks in plant			Active	Product shipped (t)	
	Aggregate	Asphalt	Total	Operations	Aggregate	Asphalt
6-13-00	483	60	543	Entire plant	13976	1399
6-14-00	358	41	399	Entire plant	10646	915
6-15-00	282	113	395	Power outage	6895	2846
6-16-00	382	54	436	Entire plant	11827	1285
6-20-00	154	33	187	Entire plant	4601	708
6-21-00	250	81	331	Entire plant	7174	1964

determined based on a calibration line (quartz peak intensity versus total mass) and the total mass absorption coefficient for the sample. The mass absorption coefficient accounted for the difference in composition between the sample and the pure quartz standard. The value was calculated based on chemical composition of the PM_{10} sample determined by proton induced X-ray emission (PIXE) prior to XRD analysis (see [9] for details).

2.3. Light detection and ranging (Lidar)

The UC Davis miniature elastic lidar instrument, described previously [15], records range-resolved elastic backscatter signals from airborne PM with high temporal (s) and spatial (5 m) resolution. Lidar two-dimensional (2D) vertical and horizontal scans were collected downwind of the sand and gravel facility between June 13 and June 16, 2000. The lidar was positioned on the SW side of the abandoned mine pit, about 430 m south of the Main Plant (see Fig. 2). Note that all lidar data are presented in terms of lidar coordinates and no correction was made for true vertical distances above the ground at each location due to the variation in topography across the site. The laser pump energy was kept constant at 6.23 J during all data collection to enable comparison between sampling days.

To obtain an overall picture of the dust distribution and propagation of the dust plumes away from the Main Plant, 2D horizontal scans were collected by scanning between 24° and 158° azimuth (see Fig. 2b) at a lidar 3° elevation angle (just above the horizon). Vertical scans were collected sequentially at up to five azimuth locations that corresponded to lines of sight (LOS) directed from the lidar to locations (Table 2): (1) downwind of the Main Plant and along the line-of-sight between the lidar and just upwind of sampler D3 (24.3° azimuth); (2) upwind of the meteorological tower (52.8°); (3) downwind of the East Gate entrance to the site (80°); (4) downwind of the D4 sampler location (102°); and (5) the southeast corner of the mine pit (158°), which was used as the lidar background scan azimuth. At the 158° azimuth, the lidar was pointed toward the southeast corner of the abandoned mine pit (denoted by grey area in Fig. 2 at 200–600 m E–W distance); plumes from the facility generally did not impact this line-of-sight during the sampling campaign. Vertical scans were performed at elevation angles from 2.5° to 23° (or 15.5°) in vertical steps of 0.25°.

Table 2
Lidar two-dimensional (2D) scan locations

Type of Lidar scan	Location relative to site markers	Azimuth (°)
2D vertical	Upwind of D3 PM sampler (D1, D2)	24
2D vertical	Upwind of Met tower	52
2D vertical	Downwind of East gate	80
2D vertical	Downwind of D4 PM sampler (D4)	102
2D vertical	SE corner of pit (far downwind) (BKG)	158
2D horizontal	Above the site, all azimuths	24–164

Vertical profiles of lidar data were obtained by averaging the lidar signal at 2 m height intervals over a specified range (distance from lidar instrument) interval that corresponded to the location of the PM point samplers. Note that all heights are relative to the lowest elevation angle (2.5°), not to actual height above the ground at a given location. The 2D vertical scans collected over the duration of a point sampler test period were averaged together to give an average profile for each sampling day. Background vertical profiles were similarly obtained from the lidar scans collected along the line of sight directed away from the source operations (158°). Maximum plume heights were recorded for all 2D vertical scans collected. Possible sources of error in measuring the maximum extent of the plume from the lidar vertical scans include the fact that some plumes extended higher than the programmed vertical limits of the lidar scan; when plumes were at very close range this problem was most severe. Another source of measurement error resulted from near field-of-view geometric optics considerations: because of the lidar's periscope arrangement, plumes within ~250 m of the lidar were not fully quantified by the lidar receiver. This limitation applies to measuring the dimensions of plumes near location D3 (~190 m from lidar); therefore, no vertical profiles were generated for location D3.

2.4. Flux and emission rate calculations

The lidar vertical profiles and wind speed data were used to estimate PM_{10} and CS mass flux at a given height up to 100 m assuming a linear relationship between the lidar backscatter signal and PM_{10} concentrations. First, the wind speed data from four heights was fit using the log-wind law, $u(z) = [u \times k] \times \ln[z/z(0)]$, in order to determine the roughness height, $z(0)$, and determine the wind speed at heights up to 100 m, $u(z)$. The lidar signal at each height in the vertical profile was converted to an estimated PM_{10} mass concentration ($\mu g\,m^{-3}$) using the linear regression equation obtained by fitting a line to the 3 m lidar data and the corresponding PM_{10} filter sample data for each sampling day. Quartz concentrations were estimated for

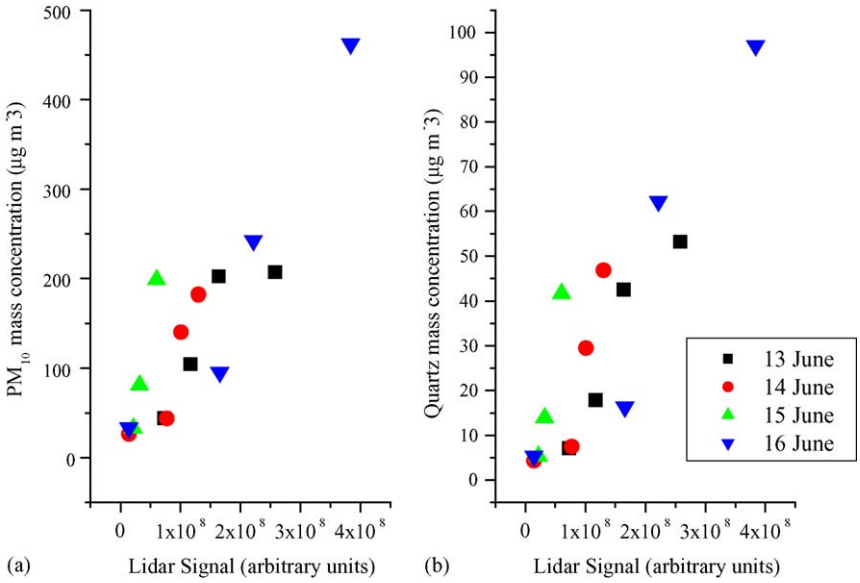

Fig. 3. Relationships between lidar signal and PM_{10} mass concentration (a) or quartz mass concentration (b) for data at 3-m height. Linear regressions to the daily points were used to estimate PM_{10} and quartz concentrations from the lidar vertical profile data.

June 13, 14, 15 using the quartz mass fractions at each sampling site determined on June 16 [9]. The linear relationships for each day explained 80–99% of the variability in the data, as determined by the R^2-value of the regressions (where y is the PM_{10} mass concentration ($\mu g\,m^{-3}$) and x is the lidar signal):

$$13\,\text{June}: y = 9 \times 10^{-7}x + 4.48, \quad R^2 = 0.78 \tag{2}$$

$$14\,\text{June}: y = 1 \times 10^{-6}x - 12.17, \quad R^2 = 0.80 \tag{3}$$

$$15\,\text{June}: y = 4 \times 10^{-6}x - 57.65, \quad R^2 = 0.99 \tag{4}$$

$$16\,\text{June}: y = 1 \times 10^{-6}x - 28.05, \quad R^2 = 0.92 \tag{5}$$

Note that due to a power outage at the site that disabled sampler D1, only three data points were used to fit the regression on June 15 (Fig. 3).

The mass flux of PM_{10} or quartz perpendicular to the lidar 2D vertical plane at a given height, z, was calculated as the product of the wind speed at that height, $u(z)$, and the PM_{10} or quartz mass concentration at that height, $C(z)$, estimated from the lidar vertical profiles. All mass flux data are reported in units of $\mu g\,m^{-2}\,s^{-1}$ and represent mass transfer perpendicular to a unit area of the lidar vertical scan plane.

Mass emission rates of PM_{10} and quartz ($\mu g\,m^{-1}\,s^{-1}$) were calculated for each downwind distance for each day of sampling by integrating the vertical flux profiles between $z(0)$ and 100 m height. This upper height was determined to be the maximum height of the fugitive dust plumes measured by the lidar as indicated by lidar signals that approached background lidar data values on most days.

3. Results and discussion

3.1. Meteorological conditions and PM mass concentrations

The wind direction, wind speed, relative humidity and temperature during the field tests were relatively similar from day to day (Table 3). Wind direction is reported on an adjusted scale of 180–540° to avoid exaggeration of the northerly wind direction when it varied between NW and NE. The mean meteorological values over the sampling test periods were generally similar (Table 3) with the exception of higher mean wind speeds on June 16. Note that mean wind direction was from the W–NW for all test periods.

The point sampler PM_{10} and quartz concentration data (Table 4) indicate the general trend of decreasing concentration with distance downwind. Recall that the sampling sites were located 22 (D1), 62 (D2), 259 (D3) and 745 m (D4) from the Main Plant indicated in Fig. 2a. The upwind sampler (U1) was 1495 m upwind and had detectable but low-PM concentrations. Sampling test period durations were varied each day, but ranged from 6.4 to 9.2 h for downwind samples and 7.1–11.4 h for upwind samples (Table 4). There was no relationship between sampling duration and total mass concentration. As confirmed by the lidar data discussed below, this observation is consistent with measurement of emissions from intermittent sources. Quartz was determined for samples collected on June 16 only and the mass fraction of quartz in the PM_{10} samples ranged from 0.16 to 0.26, with the mass fraction decreasing with distance from the Main Plant (D1 > D2 > D3 ~ D4; see [9] for more details).

3.2. Lidar profiles of plumes downwind of plant

As expected, most of the fugitive dust plumes originated from the Main Plant located about 500 m North of the lidar (see Fig. 2).

Table 3
Average test period meteorological conditions (S.D. = 1 S.D.)

Date	Height (m)	Wind dir	Wind dir S.D.	WD540	RH (%)	Solar radiatio n (W/m^2)	Temperature (°C)				Wind speed (m/s)			
		4	4	4	2	4	1	2	4	7.5	1	2	4	7.5
6/13/00	Mean	320.66	17.72	323.72	20.43	664.95	33.71	33.49	33.20	14.605	2.81	3.41	4.60	5.35
	S.D.	32.21	6.17	13.67	4.83	230.18	2.95	2.95	2.95	2.98	0.91	0.88	1.22	1.36
	n	588	588	588	588	588	588	588	588	588	588	588	588	588
6/14/00	Mean	319.10	16.44	322.37	24.13	667.39	34.83	62.963	34.39	33.86	2.96	3.53	4.77	5.54
	S.D.	33.73	5.83	15.51	5.18	228.34	4.26	4.15	4.01	3.86	0.71	0.58	0.72	0.75
	n	661	661	661	661	661	661	661	661	661	661	661	660	660
6/15/00	Mean	320.31	17.67	331.97	22.34	594.11	34.88	34.67	34.6	33.99	2.25	3.06	4.16	4.90
	S.D.	61.01	6.08	19.33	2.19	280.87	0.872	2.54	2.32	2.05	0.74	0.71	1.05	1.02
	n	494	494	494	494	494	494	494	494	494	494	494	494	494
6/16/00	Mean	311.09	14.89	311.09	22.09	566.44	30.39	30.27	329.713	29.71	3.80	4.20	5.51	6.32
	S.D.	11.79	4.22	11.79	2.73	284.28	1.66	1.56	1.2	1.24	0.72	0.64	0.92	1.06
	n	458	458	458	458	458	458	458	458	458	458	458	458	458

Table 4
Sample test periods and elapsed sampling times

Test ID	LOC	Date	Start time	End time	Duration (h)	PM_{10} ($\mu g\,m^{-3}$)	QTZ ($\mu g\,m^{-3}$)
00-003	U1	6/13/2000	0936	1954	10.38	44.15	
	D1	6/13/2000	0954	1820	8.45	207.00	
	D2	6/13/2000	1001	1830	8.48	202.27	
	D3	6/13/2000	1011	1845	8.57	75.83	
	D4	6/13/2000	1142	1915	7.55	104.57	
00-004	U1	6/14/2000	0711	1626	9.24	26.51	
	D1	6/14/2000	0723	1613	8.83	182.21	
	D2	6/14/2000	0658	1635	9.62	140.49	
	D3	6/14/2000	0740	1652	9.20	120.40	
	D4	6/14/2000	0614	1741	11.45	43.83	
00-005	U1	6/15/2000	0604	1346	7.70	32.92	
	D1	6/15/2000	No power				
	D2	6/15/2000	0720	1351	6.52	198.36	
	D3	6/15/2000	0646	1402	7.27	102.55	
	D4	6/15/2000	0636	1416	7.67	81.15	
00-006	U1	6/16/2000	0602	1310	7.13	33.41	5.38
	D1	6/16/2000	0651	1320	6.49	242.37	62.34
	D2	6/16/2000	0659	1325	6.43	462.54	97.22
	D3	6/16/2000	0637	1329	6.87	226.71	42.15
	D4	6/16/2000	0716	1339	6.38	95.57	16.32

The lidar *horizontal* scans collected at 3° elevation angle indicate that the general direction of all the plumes corresponded to the NW wind direction during the data collection period (Fig. 4a). Dust plumes originating from other nearby sources are also visible in the lidar horizontal scans (Fig. 4a). Plumes associated with traffic on the E–W road (trucks entering through E gate) appear to be significant as well. However, there was not enough horizontal scan data collected to investigate propagation of plumes originating from the unpaved road and the horizontal scans were collected at too high an elevation angle to monitor ground-level sources as well as the plant emissions. Nonetheless, it is noteworthy that the majority of plumes determined to be originating from the Main Plant did not propagate further than 400 m (East direction) from the lidar as indicated by measurement of contiguous plume lengths on horizontal scans. This observation may be a result of the data collection and analysis methods, however, and should be interpreted with caution. Horizontal scans at other elevation angles might give different plume geometries because the plumes evolve over the time the horizontal scan is collected. Also, as documented in Fig. 4a, many of the plumes had intensities that varied greatly or were discontinuous along the plume centerline (see discontinuity at *x*,*y* coordinates (0,450) in Fig. 4a). The relative intensities at the beginning and end of the continuous plumes indicate the significant temporal variability in the plumes.

The lidar average *vertical* profiles (Fig. 5) tended to vary between morning and afternoon, chiefly reflecting changes in activity at and around the Main Plant as well as variations in meteorological conditions throughout the day. For example, on June 14, the dust plumes were significantly more intense in the morning than in the afternoon (Fig. 5b). In fact, in the afternoon on June 14, only the two azimuth locations closest to the Main Plant had average lidar signals that exceeded background levels. In other words, the East gate (80°) and D4 (102°) average plume

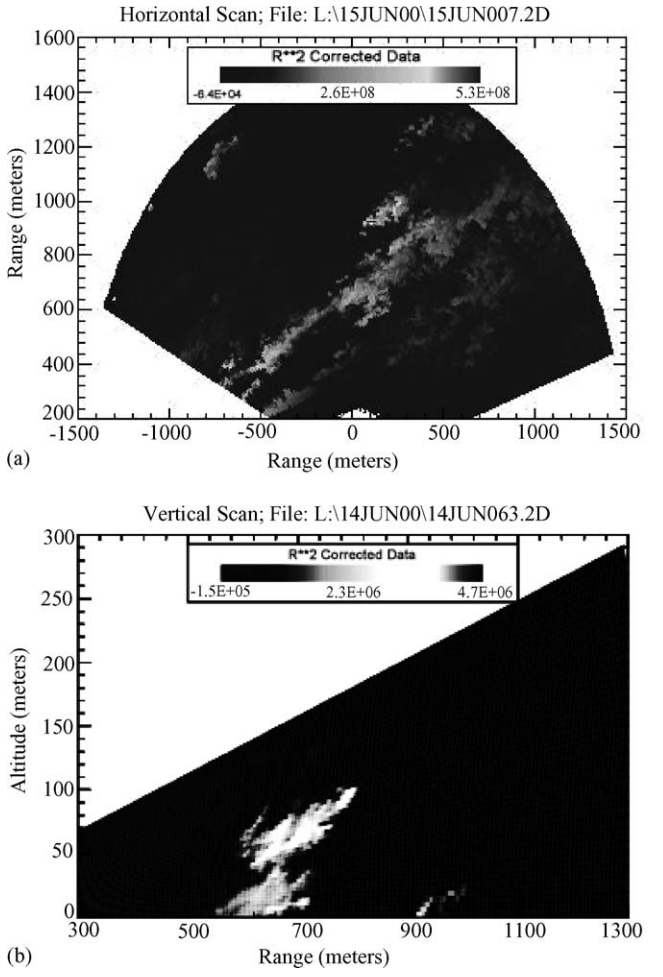

Fig. 4. Lidar two-dimensional scans. (a) Horizontal scan collected across site on June 15 at 7:30 a.m.; (b) vertical scan collected near D4 sampler location on June 14 at 8:43 a.m. Increasing whiteness in the images indicates higher lidar backscatter signal.

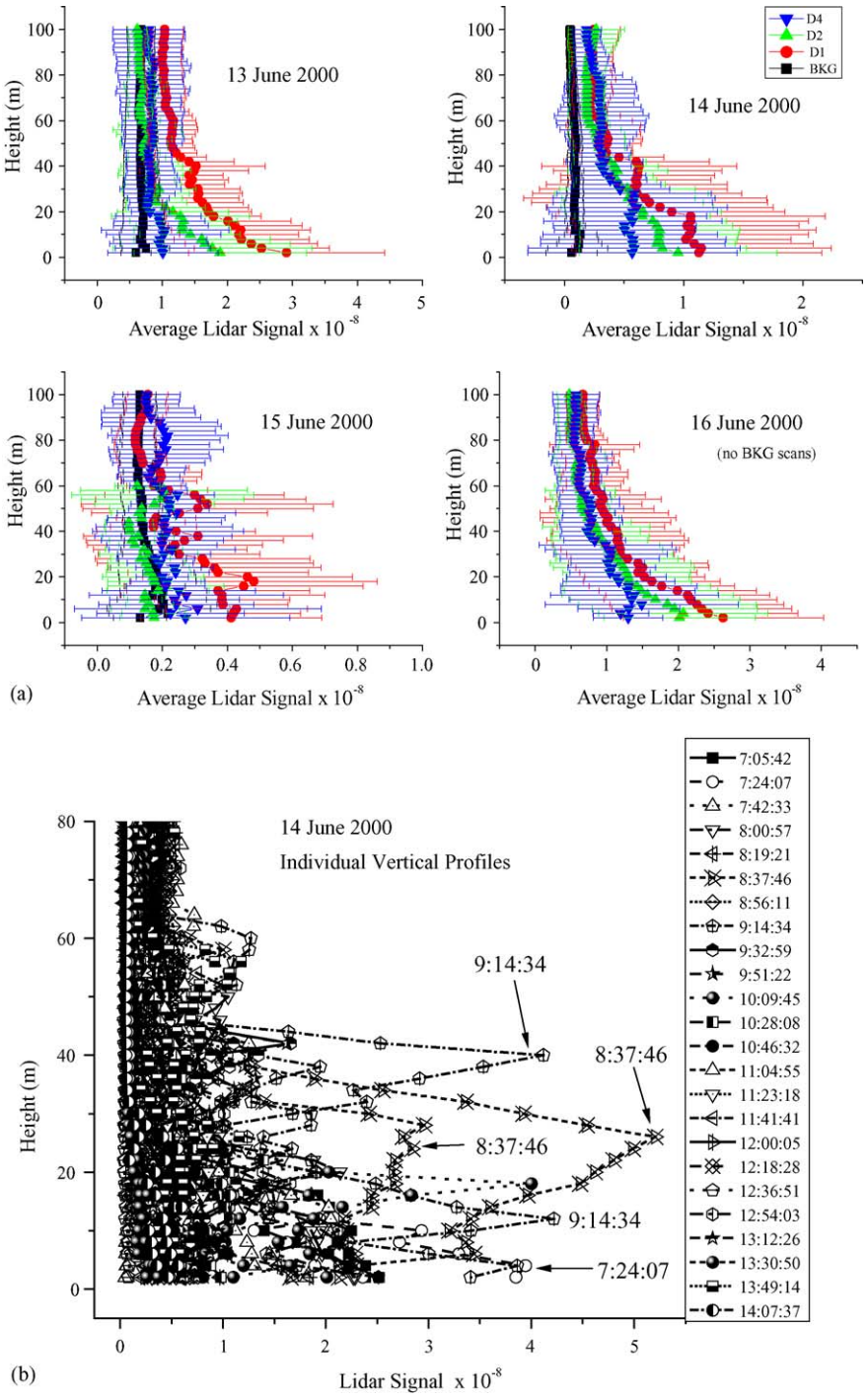

Fig. 5. (a) Vertical profiles of average lidar signals at the D1, D2, D4, and background locations over each test period (see Table 4 for times). Error bars are one standard deviation at each 2-m height interval based on the vertical scans collected over the PM test period. Background profiles (BKG) are based on lidar data collected at 158° azimuth, a LOS not impacted by the sand and gravel operation. Note that D2 vertical profile data on June 15 are truncated at 60 m height due to data recording errors and *x*-axis scales vary between panels. (b) Individual lidar scan profiles over the test period at location D1 on June 14 demonstrate the variable nature of the emissions source and differences in morning and afternoon profiles.

profiles were not significantly different from background in the afternoon on this date, but the lidar profiles collected close to the operation, at the D3 and meteorological tower azimuths, were significantly higher than background.

The relationship between the plume profile collected at the background azimuth and the other azimuths varied from day to day (Fig. 5a). Unfortunately, background files (SE pit corner) were not collected on June 16th. On June 13th and 16th, the vertical scan plume signals were higher compared to June 14th and 15th. As discussed in more detail below, this is attributed to a higher intensity of plant aggregate moving operations on those days. The background scans on June 13th show more intense

plumes than the plumes identified at the other locations. It is possible that this is due to the very high truck activity levels at both the aggregate and asphalt plants and corresponding high traffic on the two dirt access roads on June 13 relative to the other test days (see Table 1). On June 14th and 15th, the background levels were about the same with a slight change between morning and afternoon scans on June 15th.

It is important to note that the plume heights significantly exceeded the 3 m height of the PM samplers. Average plume heights determined from the lidar vertical scans ranged from approximately 25 m to over 200 m above the lowest lidar vertical scan elevation angle (2.5°). In general, the average height of the plumes, as determined from the lidar vertical scans, increased with distance from the Main Plant. This is consistent with vertical dispersion of the plumes and with rising plumes due to surface heating on these hot summer days. Average plume heights were highest at the D4 location (about 500 m from the lidar and 745 m from Main Plant) for all days. Plume heights dropped significantly at the background azimuth location, except on June 13th when a higher background lidar signal was observed.

The very high plumes generated by the Main Plant operations indicate that ground-level point samplers will be ineffective in capturing all of the PM emissions from these types of operations. Therefore, techniques such as lidar that enable estimates of PM concentrations at heights that are impractical for point sampling will give more representative flux and emission rate values for the facility.

The average vertical profiles shown in Fig. 5a are relatively smooth functions of height due to the fact that they average over 6–8 h of sampling time (see Table 4 for actual time periods). The large error bars at each height interval attest to the true variability in the lidar backscatter signal between the individual 1-min lidar scans. It is also interesting to note that the average lidar signal was generally high at the lower measurement heights and decreased with height, with occasional increases in intensity due to elevated plumes, such as the one captured in Fig. 4b above ~50 m height. The elevated plumes are most obvious on the June 15 vertical profile at D1 where sustained plumes at ~15, 35, and 50 m height were detected (Fig. 5). Similarly, at location D4 (745 m downwind from Main Plant), an elevated plume was detected at ~80 m height, but at a much lower concentration than the lower elevation plumes.

3.3. Lidar-based off-site fluxes of PM and quartz

Average vertical profiles of PM_{10} flux, the product of wind speed and concentration (based on lidar vertical profiles), are shown in Fig. 6 for each day of sampling. For all days, the maximum flux was generally observed at sampling location D1 and was greatest at heights between 10 and 20 m. The D2 and D4 location flux profiles for June 13, 14, and 16 show higher D2 fluxes near the ground (<30 m) and higher D4 fluxes at the higher elevations (heights > 30 m). These relationships are in good agreement with what one would predict for a ground-based source dispersing under convective conditions. The D2 data for June 15 were not significantly different from background. This was likely due to the power outage at the Main Plant on this day that prevented collection of a PM sample at location D1 (the D1 sampler used Main Plant line power) and also restricted activity at the Main Plant to use of mobile earth-moving equipment for transporting the piles of sand and gravel (no stationary conveyors or crushers operated this day). Note that the PM fluxes were greatest on June 16, the day with the highest recorded wind speeds and no distinguishable elevated dust plumes as indicated

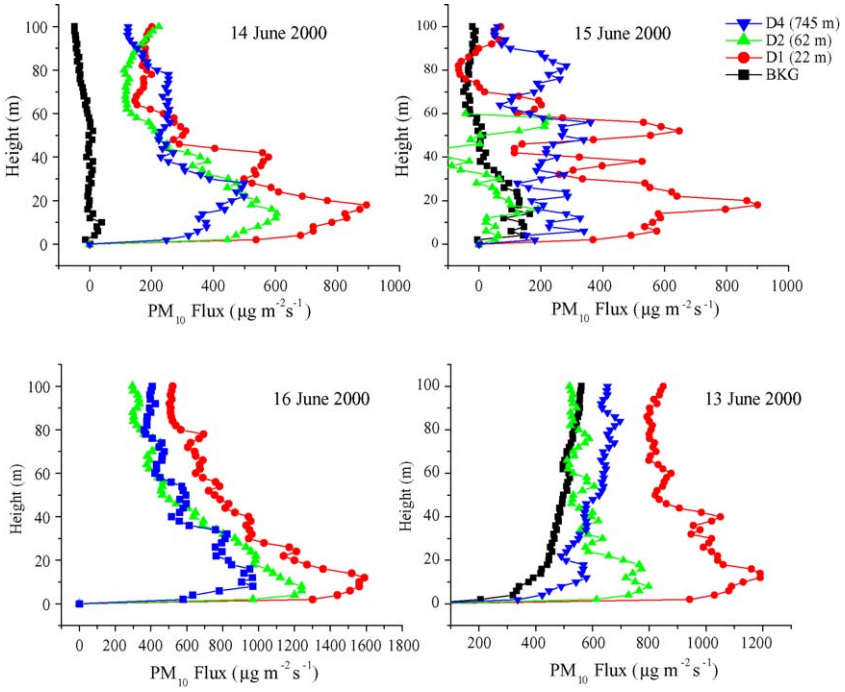

Fig. 6. Vertical profiles of PM_{10} flux based on average lidar signal, daily PM_{10}–lidar signal linear relationships and wind speed at 2-m intervals.

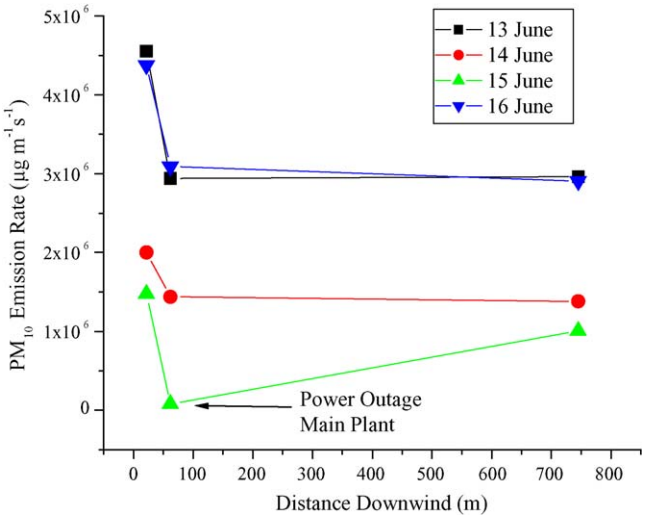

Fig. 7. PM_{10} emission rates estimated from lidar vertical profiles averaged over each sampling day as a function of downwind distance from Main Plant.

by the very smooth flux profiles at all three locations. This result may indicate the influence of mechanical turbulence on the PM vertical profiles: it tends to smooth out the average profiles due to intense mixing.

Emission rates calculated by integrating the flux profiles in Fig. 6 give an estimate of the total mass of PM_{10} and quartz emitted per unit meter width of the operation that is perpendicular to the lidar scan plane. Fig. 7 shows that there were two groups of emission rate days. June 13 and 16 had very similar emission rates that were much higher than the emission rates measured at D1, D2, and D4 on June 14 and 15. The low-emission rate calculated for June 15 at location D2 can be attributed to the power outage at the Main Plant that curtailed activity near D2 on that day only. The emission rates decreased dramatically with distance from locations D1 (22 m) to D2 (62 m downwind) and then leveled off, with no difference from location D2 to D4 on three of the four sampling days. These results contrast with the trends with downwind distance that one typically observes for sampling PM at a single height, where mass decreases continually with downwind distance. The patterns in Fig. 7 suggest little net settling out of airborne PM_{10} occurred between 65 and 745 m from the Main Plant. Alternatively, the observed truck travel on the unpaved roads between D2 and D4 contributed additional PM_{10} to the samples collected at D4. In other words, explaining the shape of the emission rate as a function of downwind distance from the Main Plant (Fig. 7) is complicated by the complex nature of the large area source with multiple smaller areas that generate airborne geologic dust.

Differences in truck and plant activity between days (see Table 1) account for the similar magnitudes of the emission rates on June 13 and 16 compared to June 14 and 15. June 13 was the day with the most truck and facility processing activity, followed by June 16. June 14 and 15 had about the same number of trucks entering the facility, but June 14 had a significantly higher mass of product shipped, likely due to the power outage on June 15 curtailing facility activity. Linear regressions of PM emission rates with respect to all the activity variables (see

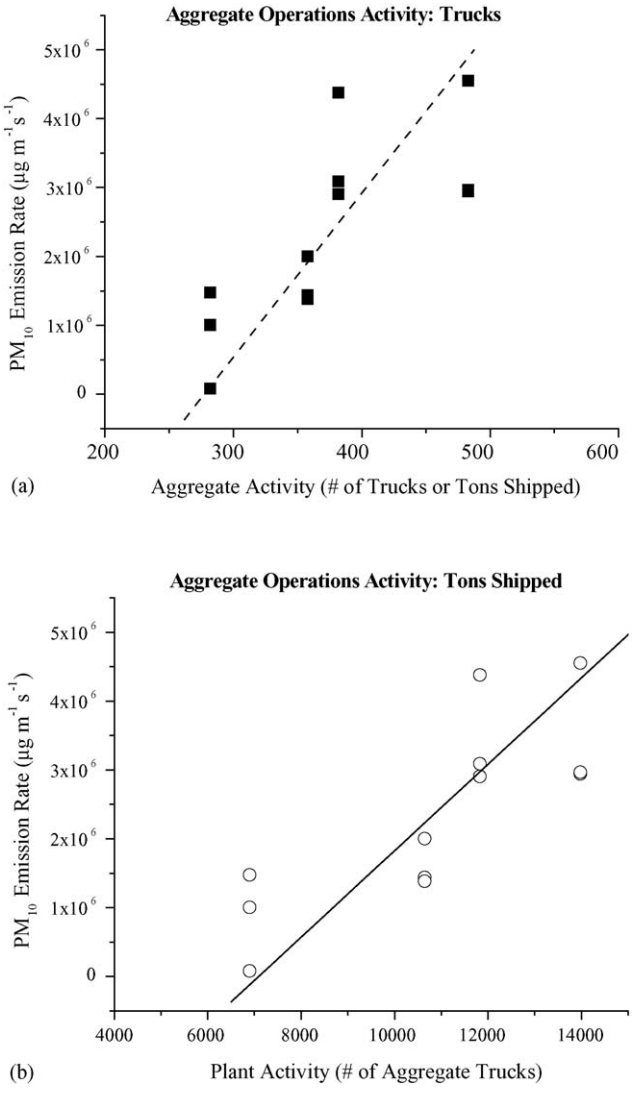

Fig. 8. Relationships between PM_{10} emission rates estimated from lidar data and two measures of activity at the facility based on data in Table 1: (a) number of aggregate trucks on the site and (b) tons of aggregate product shipped.

Table 1) and meteorological variables (see Table 3) showed that 71–86% of the variability in emission rates could be explained by the number of *aggregate* trucks and the tons of *aggregate* shipped per day (Fig. 8). All of the other variables did not correlate with PM_{10} emission rate. The lower correlation coefficient for total trucks ($R^2 = 0.64$) compared to that for aggregate trucks alone ($R^2 = 0.72$) suggests a stronger dependence on the number of aggregate trucks at the facility. The importance of collecting ancillary data on the most relevant parameters that govern the PM emissions at these types of facilities is essential to developing better predictive emission factor models at these complex sites. Furthermore, both the temporal and spatial location of dust-generating activities becomes more important to interpretation of PM concentration data collected with instruments such as the lidar.

The emission rates reported in Fig. 7 were normalized to tons of aggregate product shipped and the number of aggregate trucks on the property to give emission factors for sand and

Table 5
PM_{10} and quartz emission factor estimates based on PM_{10} quartz mass fraction, lidar and two facility activity measures

	PM_{10} and quartz emission factors[a]					
	6/13/00	6/14/00	6/15/00	6/16/00	Mean	S.D.
PM_{10} (total # trucks) (kg/truck)						
BKG	71	−2	6	–	25	40
D1	136	80	75	165	114	44
D2	88	58	4	116	66	48
D4	88	56	51	110	76	28
PM_{10} (total tons shipped) (kg/t)						
BKG	2.4	−0.1	0.3	–	1	1
D1	4.7	2.7	3.1	5.3	4	1
D2	3.0	1.9	0.2	3.8	2	2
D4	3.1	1.9	2.1	3.5	3	1
Quartz (total # trucks) (kg/truck)						
BKG	11.4	−0.3	1.0	–	4	6
D1	34.9	20.7	19.4	42.4	29	11
D2	18.4	12.1	0.9	24.5	14	10
D4	15.1	9.5	8.8	18.7	13	5
Quartz (total tons shipped) (kg/t)						
BKG	0.39	−0.01	0.04	–	0.14	0.22
D1	1.21	0.70	0.79	1.37	1.02	0.32
D2	0.64	0.41	0.03	0.79	0.47	0.33
D4	0.52	0.32	0.36	0.60	0.45	0.13

[a] Assumes 8-h operation and 500 m facility boundary width; units = kg/truck or kg/t product.

gravel operations. Similarly, the PM_{10} mass data were converted to quartz mass concentration using the mass fraction of quartz in PM_{10} samples to estimate quartz emission factors. The PM_{10} and quartz emission factors calculated on the basis of both the number of trucks at the facility and the tons of product shipped are shown in Table 5.

4. Conclusions

This study applied measured relationships between the average lidar signal and time-integrated filter-based PM_{10} measurements at a single height to estimate the overall flux and emission factors for PM_{10} and quartz from a sand and gravel facility in Central California during the hot, dry summer season. Average emission factors on the order of 65–110 kg of PM_{10} (10–30 kg quartz) per daily truck activity or 2–4 kg/t product shipped (0.5–1 kg quartz/t) were quantified for this facility. While the study results demonstrate that techniques such as lidar that enable estimates of PM emissions at heights that are impractical for point sampling will give more spatially representative flux and emission rate values for the facility, these data must be interpreted with caution for several reasons. First, the lidar signal–PM_{10} relationship varied between days and is a function of atmospheric scattering properties. Therefore, future application of lidar to estimating PM emission factors will require detailed quantification of the ability of these relationships to provide meaningful data under a wide range of environmental conditions. It is also important to collect background lidar scans at locations upwind of the site—a situation not logistically possible in this study. Vertical arrays of point samplers should be employed to verify the PM_{10}–lidar signal relationships at 3 m apply at all heights. Second, the emission rates likely represent worst-case values because the field sampling was carried out during the summer. Emissions during the wet winter season are expected to make considerably lower contributions to an emissions factor based on year-round facility operation.

This study has important implications for airborne CS concentrations downwind of sand and gravel operations, especially given the detection of significant PM_{10} and corresponding CS at elevated heights downwind. The PM_{10} flux measured at heights above 30 m at D4, 745 m downwind of the Main Plant, represent significant transport of PM_{10} off-site and are of potentially significant cause for concern to downwind sensitive receptors. While the ground-based (3 m height) point sampler measurements approached background quartz values at this downwind distance [9], the off-site flux of plumes reaching higher elevations, as detected by lidar, suggest that future studies should employ lidar to track these plumes until the lidar signal approaches background levels to determine long-range downwind transport distances.

Acknowledgments

The authors thank the California Air Resources Board under contract 98-348 (N. Motallebi) and R. Flocchini at Crocker Nuclear Laboratory, UC Davis, for financial support of this work.

References

[1] B. Fubini, Health effects of silica, in: A.P. Legrand (Ed.), The Surface Properties of Silicas, 1998, pp. 415–470.
[2] A.B. Kane, Questions and controversies about the pathogenesis of silicosis, in: V. Vallyathan (Ed.), Silica and Silica-induced

Lung Diseases: Current Concept, CRC Press, Boca Raton, FL, 1996.
[3] B.J. Williamson, S. Pastiroff, G. Cressey, Piezoelectric properties of quartz and cristobalite airborne particulates as a cause of adverse health effects, Atmos. Environ. 35 (20) (2001) 3539–3542.
[4] IARC, Monographs on the Evaluation of Carcinogenic Risks to Human. Silica, Some Silicates, Coal Dust and Para-aramid Fibril, International Agency for Research on Cancer, 1997, p. 506.
[5] B.L. Davis, Quantitative analysis of crystalline and amorphous airborne particulates in the Provo-Orem vicinity, Utah Atmos. Environ. 15 (1981) 613–618.
[6] B.L. Davis, et al., The quartz content and elemental composition of aerosols from selected sites of the EPA inhalable particulate network, Atmos. Environ. 18 (4) (1984) 771–782.
[7] S. Puledda, L. Paoletti, M. Ferdinandi, Airborne quartz concentration in an urban site, Environ. Pollut. 104 (1999) 441–448.
[8] M.J. Nieuwenhuijsen, et al., Personal exposure to dust, endotoxin and crystalline silica in California agriculture, Ann. Occup. Hyg. 43 (1) (1999) 35–42.
[9] R. Shiraki, B.A. Holmén, Airborne respirable silica near a sand and gravel facility in Central California: XRD and elemental analysis to distinguish source and background quartz, Environ. Sci. Technol. 36 (23) (2002) 4956–4961.
[10] H.C. van de Hulst, Light Scattering by Small Particles, Dover Publications, New York, 1981.
[11] R.M. Measures, Laser Remote Sensing, Wiley Interscience, New York, 1984, p. 510.
[12] V.A. Kovalev, W.E. Eichinger, Elastic Lidar: Theory, Practice and Analysis Methods, John Wiley & Sons, Inc., Hoboken, NY, 2004, p. 615.
[13] R.A. Eldred, et al., IMPROVE—A new remote area particulate monitoring system for visibility studies, in: Air Pollution Control Association 81st Annual Meeting, Dallas, TX, 1988.
[14] W. John, G. Reischl, A cyclone for size-selective sampling of ambient air, APCA J. 30 (1980) 872–876.
[15] B.A. Holmén, W.E. Eichinger, R.G. Flocchini, Application of elastic lidar to PM_{10} emissions from agricultural nonpoint sources, Environ. Sci. Technol. 32 (1998) 3068–3076.